Structure formation in parallel ion flow and density profiles by cross-ferroic turbulent transport in linear magnetized plasma

Cite as: Phys. Plasmas **23**, 102311 (2016); https://doi.org/10.1063/1.4965915
Submitted: 12 July 2016 • Accepted: 10 October 2016 • Published Online: 28 October 2016

T. Kobayashi, S. Inagaki, Y. Kosuga, et al.

Structure formation in parallel ion flow and density profiles by cross-ferroic turbulent transport in linear magnetized plasma

T. Kobayashi,[1,a)] S. Inagaki,[2,3] Y. Kosuga,[2,3,4] M. Sasaki,[2,3] Y. Nagashima,[2,3] T. Yamada,[3,5] H. Arakawa,[6] N. Kasuya,[2,3] A. Fujisawa,[2,3] S.-I. Itoh,[2,3] and K. Itoh[1,3]
[1]*National Institute for Fusion Science, National Institutes of Natural Sciences, Gifu, Japan*
[2]*Research Institute for Applied Mechanics, Kyushu University, Fukuoka, Japan*
[3]*Research Center for Plasma Turbulence, Kyushu University, Fukuoka, Japan*
[4]*Institute for Advanced Study, Kyushu University, Fukuoka, Japan*
[5]*Faculty of Arts and Science, Kyushu University, Fukuoka, Japan*
[6]*Teikyo University, Fukuoka, Japan*

(Received 12 July 2016; accepted 10 October 2016; published online 28 October 2016)

In this paper, we show the direct observation of the parallel flow structure and the parallel Reynolds stress in a linear magnetized plasma, in which a *cross-ferroic turbulence* system is formed [Inagaki *et al.*, Sci. Rep. **6**, 22189 (2016)]. It is shown that the parallel Reynolds stress induced by the density gradient driven drift wave is the source of the parallel flow structure. Moreover, the generated parallel flow shear by the parallel Reynolds stress is found to drive the parallel flow shear driven instability D'Angelo mode, which coexists with the original drift wave. The excited D'Angelo mode induces the inward particle flux, which seems to help in maintaining the peaked density profile. *Published by AIP Publishing*. [http://dx.doi.org/10.1063/1.4965915]

I. INTRODUCTION

Self-organization of flow structures observed in fusion and fundamental plasmas is one of the central issues in physics of complex systems.[1,2] A typical example is the spontaneous toroidal flow formation in torus plasmas, the so-called intrinsic rotation.[3–5] The toroidal plasma rotation is one of the key elements for realizing a sufficiently high β plasma for fusion reactors, since that suppresses some MHD modes that can induce disruptions.[6] Even in low temperature linear plasmas, complicated parallel flow structures including the parallel flow reversal are routinely observed.[7–9] Despite continuous and intensive studies, the generation mechanism of the intrinsic plasma rotation is still not fully understood. One of the candidates is regarded to be the turbulent momentum transport, i.e., the parallel Reynolds stress.[10,11] Direct measurement of the parallel Reynolds stress has been performed in various fusion and fundamental plasma devices.[12–16] However, quantitative demonstration that shows the critical role of the parallel Reynolds stress on the parallel flow structure formation has not yet been achieved.

The flow shear structure can also be a source of turbulence and turbulent transport. In particular, the parallel flow shear driven instability is called the D'Angelo mode,[17] whose basic characteristics are investigated in a linear plasma.[18] Coupling between flow shear driven instabilities and the particle flux is reported, showing a possible off-diagonal transport channel.[12,19,20] Comprehensive illustration of the multi-channel transport system, which we call the *cross-ferroic turbulence* system,[21] is mandatory.

In this paper, we show the results of the direct measurement of the parallel flow structure and the parallel Reynolds stress in a linear magnetized plasma, in which a complicated parallel flow structure is formed. It is shown that the parallel Reynolds stress induced by the density gradient driven drift wave is the source of the parallel flow structure. Moreover, the parallel flow shear generated by the parallel Reynolds stress is found to drive the parallel flow shear driven instability D'Angelo mode,[17,18] which coexists with the original drift wave.[22] The excited D'Angelo mode induces the inward particle flux, which seems to help in maintaining the peaked density profile. The structure formation in the parallel flow profile and the density profile is discussed in the case where the drift wave and the D'Angelo mode coexist forming the cross-ferroic turbulent state.

The paper is organized as follows. The experimental setup is explained in Section II, after which the fundamental observations, such as the parallel flow structure, the density profile, and the turbulence spectra, are introduced in Section III. Section IV is dedicated for the analysis of the parallel flow structure driven by the parallel Reynolds stress using the parallel momentum conservation equation. In Section V, coexistence of the drift wave and the D'Angelo mode is demonstrated, in addition to the stability analysis of the D'Angelo mode. Discussion and summary are presented in Sections VI and VII, respectively.

II. EXPERIMENTAL SETUP AND DATA ANALYSIS METHOD

The experimental observations are performed in the linear magnetized plasma, the Plasma Assembly for Nonlinear Turbulence Analysis (PANTA). The cylindrical plasma typically has a length of $l = 4$ m and a radius of $a = 50$ mm. A helicon plasma source is located at one side of the vessel, where a double loop antenna on the quartz tube with a length of 400 mm and a diameter of 100 mm is equipped.[23] Argon gas is fed in the quartz tube, where the neutral

[a)]E-mail: kobayashi.tatsuya@LHD.nifs.ac.jp

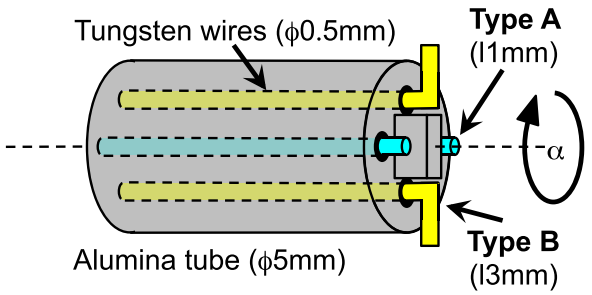

FIG. 1. Schematic view of the Mach probe array.

pressure is monitored with an ionization gauge. The neutral gas is ionized by the rf discharge with 3 kW and 7 MHz in the quartz tube. On the other side of the vessel, the plasma is terminated by the end-plate made of stainless steel. Near the end-plate, two main turbomolecular pumps exhaust the neutral gas. Two baffle plates having an annular shape with an inner diameter of 150 mm are installed at the source region and the end-plate region in order to keep the neutral pressure constant in the region between them. Homogeneous axial (z) magnetic field of $B = 0.09$ T, which is directed from the source region to the end-plate region, confines plasma in the radial direction (r). The azimuthal direction (θ) is defined as the right-handed screw direction of z, which corresponds to the electron diamagnetic direction. Despite the toroidal devices, there is no symmetry along the magnetic field, and a mean gradient of plasma parameters exists. The density gradient lengths of the radial direction and the axial direction correspond to the scale of the plasma column, i.e., $L_r \sim a \sim \mathrm{O}(10\,\mathrm{mm})$ and $L_z \sim l \sim \mathrm{O}(1000\,\mathrm{mm})$, respectively. The typical plasma parameters are as follows: the electron density of $n_e \sim 1 \times 10^{19}\,\mathrm{m}^{-3}$, the electron temperature of $T_e \sim 3\,\mathrm{eV}$, and the ion temperature of $T_i \sim 0.1 \times T_e$. The typical discharge duration is 500 ms, from which the later saturated time period of 290 ms is used for the analysis. The mean quantity and the fluctuation quantity for an arbitrary variable ψ are defined as $\bar{\psi} \equiv \langle \psi \rangle$ and $\tilde{\psi} \equiv \psi - \bar{\psi}$, respectively, where $\langle * \rangle$ denotes the time average for the period of 290 ms. This time period is about 1000 times longer than the typical turbulence period.

A schematic view of the Mach probe array used here is shown in Fig. 1. An insulation tube made of alumina with a diameter of 5 mm houses two types of tungsten probe tips noted as A and B, which are arranged alternately. The diameter of the probe tips is 0.5 mm. The A tips measure the plasma velocity as a Mach probe system, while the B tips measure the floating potential ϕ_f. The probe head is rotatable with the rotation axis in the radial direction in order to perform the calibration experiment. Here, the rotation angle $\alpha = 0$ corresponds to the angle in which the A tips align in the magnetic field direction. The axial flow velocity can be measured with $\alpha = 0°$ or 180°, while the azimuthal flow velocity can be measured with $\alpha = 90°$ or 270°. The probe head can be radially moved in the range $r > 20$ mm, without disturbing the plasma. In this set of experiments, the radial profile of the plasma parameters are measured at six different axial positions using a sole probe [see horizontal dashed lines in Fig. 2]. The probe is replaced when the vacuum vessel is opened. The reproducibility of the discharge before and after the vacuum vessel opening is sufficiently high, which is checked with a monitor reference probe.

The plasma flow velocity is analyzed with the ion currents at the up stream side (I_u) and the down stream side (I_d) as $V_z = c_s \sqrt{T_e/2T_i}\,[I_u - I_d]/I_{is}$,[24–26] where $c_s \equiv \sqrt{T_e/m_i}$ is the ion sound velocity ($T_e \gg T_i$ in the PANTA plasma) and I_{is} is the ion saturation current evaluated as $I_{is} = I_u + I_d$. The ion sound velocity in PANTA is $c_s \sim 2$–$3\,\mathrm{km/s}$. Another

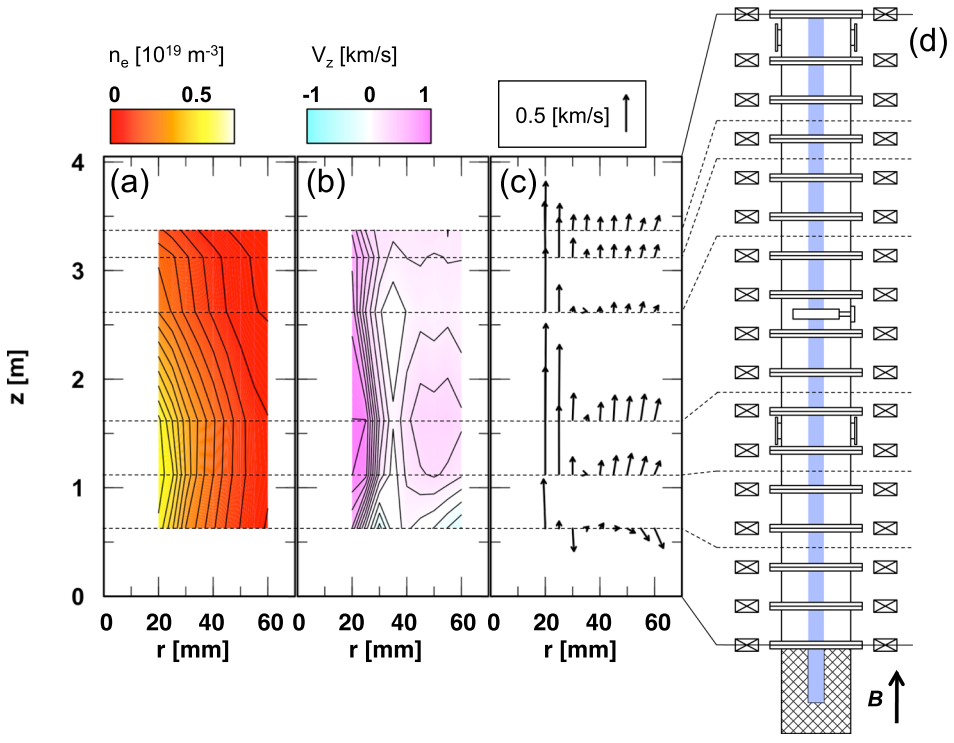

FIG. 2. Mean profiles of (a) the electron density, (b) the axial ion velocity, and (c) the velocity vector, and (d) schematic view of the PANTA device. Dashed horizontal lines show the measurement axial locations.

model to evaluate the flow velocity, $V_z = c_s^2/4v_{th,i}\ln[I_u/I_d]$,[27] where $v_{th,i}$ is the ion thermal velocity given as $v_{th,i} \equiv \sqrt{T_i/m_i}$, is also examined, and quantitatively similar results are obtained. The radial profile of $\bar{V}_z$ measured with the Mach probe results in a reasonable agreement with that evaluated with the *time delay estimation*.[8] The relative density fluctuation is evaluated as the relative ion saturation current fluctuation as $\tilde{n}_e/\bar{n}_e = \tilde{I}_{is}/\bar{I}_{is}$. The azimuthal electric field is obtained from the measured floating potential difference $\Delta\phi_f$ as $E_\theta = -\Delta\phi_f/d_B$, where $d_B \sim 5.5$ mm is the center-distance between the B tips. The electron temperature profile is measured with the B tips using the double probe method.

In order to obtain reasonable results with the Mach probe measurement, differences in characteristics of the A tips, e.g., the surface area and the shunt resistance, have to be compensated for. Probe angle rotation with 180° can exchange the probe tips at the up stream side and the down stream side. The calibration coefficients are obtained taking the ratio of the mean up stream ion currents (or the mean down stream ion current) measured with $\alpha = 0°$ and 180°. Furthermore, in order to confirm the reliability of the results, in particular, for the higher order values such as the parallel momentum flux, all of the experiments performed with $\alpha = 0°$ are repeated with $\alpha = 180°$. The error bar in the article is evaluated based on the difference between the measurements with $\alpha = 0°$ and 180°.

The parallel momentum transport in the radial direction, here we call the parallel Reynolds stress, is calculated as[10,11]

$$\Pi_{rz} = \langle \tilde{V}_z \tilde{V}_r \rangle + \bar{V}_z \langle \tilde{V}_r \tilde{n}_e/\bar{n}_e \rangle + \langle \tilde{V}_z \tilde{V}_r \tilde{n}_e/\bar{n}_e \rangle, \quad (1)$$

where the radial velocity fluctuation is defined as the $E \times B$ velocity $\tilde{V}_r = \tilde{E}_\theta/B$. The first, second, and third terms in Fig. 1 are called the velocity correlation term, the convective term, and the triple correlation term, respectively. Here, the velocity correlation term is denoted as

$$\Pi_{rz}^{VV} = \langle \tilde{V}_z \tilde{V}_r \rangle. \quad (2)$$

The convective term is the pinch term caused by the turbulent particle transport

$$\Gamma_r = \langle \tilde{V}_r \tilde{n}_e \rangle. \quad (3)$$

Even with the azimuthal symmetry providing $\bar{E}_\theta = 0$, fluctuations can induce an effective mean radial velocity as

$$\bar{V}_r = \Gamma_r/\bar{n}_e. \quad (4)$$

III. FUNDAMENTAL OBSERVATIONS

Figure 2 shows the radial-axial (r–z) profiles of the electron density, the parallel flow velocity, and the flow vector projected in the r–z plane. The electron density profile has a peak at $r < 20$ mm and $z = 1.1125$ m, and gradually decays in the radial and axial directions with specific scales a and l, respectively. The parallel flow structure is much more complicated. In the radially central region $r \sim 20$ mm, a strong parallel flow is observed. The radial profile is not a simply decaying shape with radius, but has a dent at the mid-radius $r \sim 30$ mm. A flow reversal is even observed at $r = 30$ mm and $z = 0.625$ m. As a result, a large flow shear is formed there. The plasma flow is mainly directed in the axial direction with the typical order difference of $O(\bar{V}_z)/O(\bar{V}_r) \sim 10$. As the axial length of the plasma is 100 times longer than the plasma radius, the main plasma loss channel is in the radial direction. Figure 3 shows the inverse effective particle confinement time in both the axial direction $\bar{V}_z/l$ and the radial direction $\bar{V}_r/a$. Therefore, the density profile seems to be predominantly determined by the cross field turbulent flux.

A perspective view of the turbulent fluctuations at $z = 0.625$ m, where the flow reversal is observed at $r = 30$ mm, can be seen in Fig. 4. The top three panels show the radial profiles of the normalized power spectrum density of the azimuthal electric field fluctuation $\tilde{E}_\theta/Bc_s$, the density fluctuation $\tilde{n}_e/\bar{n}_e$, and the parallel velocity fluctuation $\tilde{V}_z/c_s$, respectively. Although the peak frequencies are similar among them, i.e., $f = 1.4$, 2.8, 4.2, and 6.4 kHz, the radial profiles of the power spectra differ significantly. For instance, the azimuthal electric field spectrum has a weak fluctuation power at $r = 30$ mm, but the density fluctuation does not. The observed fluctuations therefore are not a simple drift wave that satisfies the Boltzmann relation. Figure 4(d) shows the squared cross coherence between the azimuthal electric field fluctuation and the density fluctuation $\gamma^2_{n_e,E_\theta}$. Although the eigenfunctions are different, the coherence is high, in particular, at the frequency peaks.

As the fluctuations have a coherence, a turbulence driven cross field flux on either the particle or the parallel momentum is expected. The frequency resolved spectra of the particle flux and the parallel momentum flux (the velocity correlation term) are defined as

$$\Gamma_r(f) = \frac{1}{B}\sqrt{\gamma^2_{n_e,E_\theta} S_{n_e} S_{E_\theta}} \cos\eta_{n_e,E_\theta}, \quad (5)$$

and

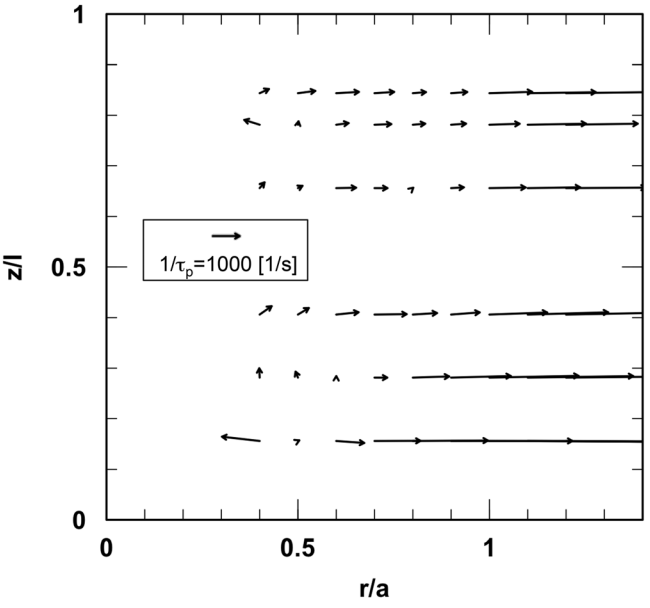

FIG. 3. Vector field of $1/\tau_p$.

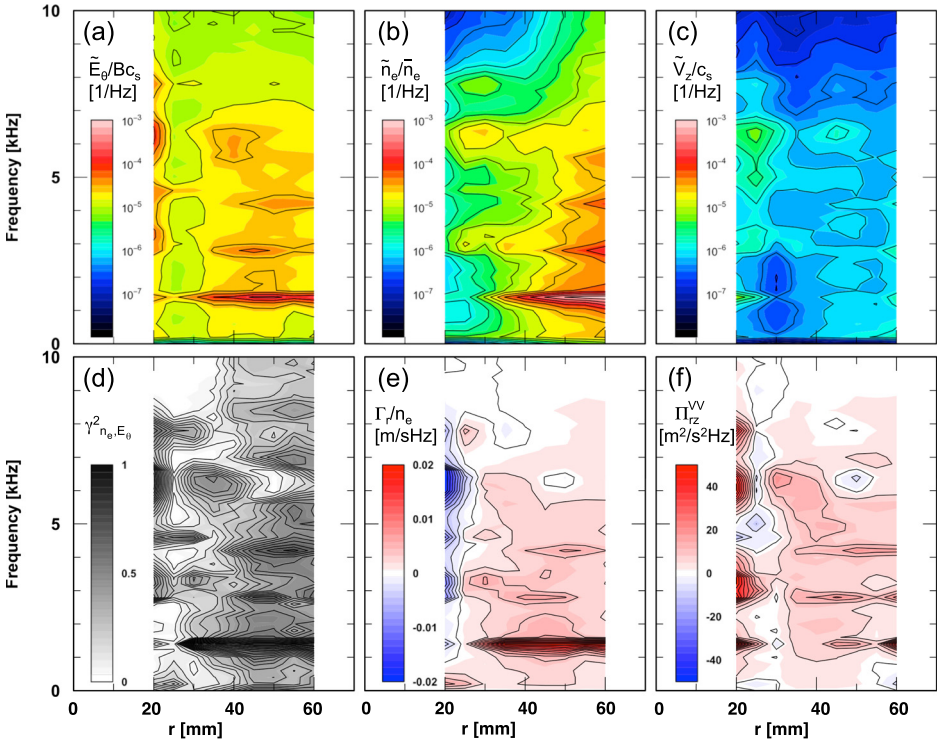

FIG. 4. Radial profiles of frequency spectra for (a) the relative azimuthal electric field fluctuation, (b) the relative electron density fluctuation, (c) the relative axial velocity fluctuation, (d) the squared cross coherence between the azimuthal electric field fluctuation and the electron density fluctuation, (e) the particle flux, and (f) the radial-azimuthal momentum flux at $z = 0.625$ m.

$$\Pi^{VV}_{rz}(f) = \frac{1}{B}\sqrt{\gamma^2_{V_z,E_\theta} S_{V_z} S_{E_\theta}}\cos\eta_{V_z,E_\theta}, \tag{6}$$

respectively. The power spectrum densities of the azimuthal electric field fluctuation $\tilde{E}_\theta$, the electron density fluctuation $\tilde{n}_e$, and the parallel flow fluctuation $\tilde{V}_z$ are given as S_{E_θ}, S_{n_e}, and S_{V_z}, respectively. The spectral correlation analysis provides the squared cross coherence and the phase difference between $\tilde{n}_e$ and $\tilde{E}_\theta$ (noted as $\gamma^2_{n_e,E_\theta}$ and η_{n_e,E_θ}) and those between $\tilde{V}_z$ and $\tilde{E}_\theta$ (noted as $\gamma^2_{V_z,E_\theta}$ and η_{V_z,E_θ}). Figure 4(e) indicates the particle flux spectrum normalized by the electron density, $\Gamma_r(f)/n_e$. At the radius where the electric field fluctuation spectrum has a gap, i.e., $r = 25$ mm, the polarity of the particle flux turns over from negative (inward) to positive (outward). The linearly unstable drift wave intrinsically provides a weak outward convective particle flux. Therefore, the fluctuation at $r < 25$ mm is caused by the other instabilities. Previous dedicated studies for identification of the instability revealed that the fluctuation at $r > 25$ mm and $f \sim 3$ kHz and 6 kHz can be classified as the resistive drift wave.[28–30] In addition, the coherent low frequency mode ($f = 1.4$ kHz), and its harmonics ($f = 2.8$, 4.2,… kHz) correspond to the nonlinearly excited mode from the drift waves, the so-called *mediators*. The mediators are regarded to play an essential role to form the nonlinear convective transport cell *streamers*.[31] The parallel momentum transport shown in Fig. 4(f) also has a gap at $r = 25$ mm, but the direction of the transport is outward in nearly all radial and frequency regions shown here.

IV. FLOW STRUCTURE FORMATION BY THE PARALLEL REYNOLDS STRESS

In order to analyze the turbulent momentum flux that excites the global flow structure, the parallel Reynolds stress defined in Eq. (1) is calculated. The radial profiles of the parallel Reynolds stress as well as each term in Eq. (1) for different axial positions, $z = 0.625$ m, 1.125 m, 1.625 m, and 2.625 m, are shown in Figs. 5(a)–5(d), respectively. The velocity correlation term $\langle \tilde{V}_z \tilde{V}_r \rangle$ dominates over the other two terms except for the case of $z = 0.625$ m, where all three terms have the same order of magnitude.

Negative divergence of the Reynolds stress gives the net influx of the momentum at a certain location, which corresponds to the driving force of the flow. The important role of the parallel Reynolds stress on maintaining the parallel flow structure can be demonstrated by examining the steady state equation of motion, i.e., the force balance equation. This is given as

$$0 = -V_z\frac{\partial V_z}{\partial z} - V_r\frac{\partial V_z}{\partial r} - \frac{\partial p}{\partial z} - m_i n_i \frac{\partial r\Pi}{r\partial r} - m_i n_i \nu_{in} V_z, \tag{7}$$

where p is the total pressure $p_e + p_i$, i.e., the sum of the electron pressure and the ion pressure, m_i is the ion mass, and ν_{in} is the ion-neutral collision frequency. The ion density n_i is considered to be equal to the electron density n_e due to the quasi-neutrality. Terms in the r.h.s. are called the inertia terms from the axial and radial derivatives, the pressure term, the parallel Reynolds stress term, and the neutral drag term. The first four terms correspond to the flow excitation force, and the last term is the drag force that balances the excitation force. Radial profiles of the first four terms are given in Figs. 5(e)–5(h) for different axial positions, where two inertia terms are combined. Except for the case $z = 2.625$ m, the parallel Reynolds stress term dominates over the other terms. In addition, the spatial structure of the parallel Reynolds stress term resembles the parallel flow profile that has a dent at $r \sim 3$ cm.

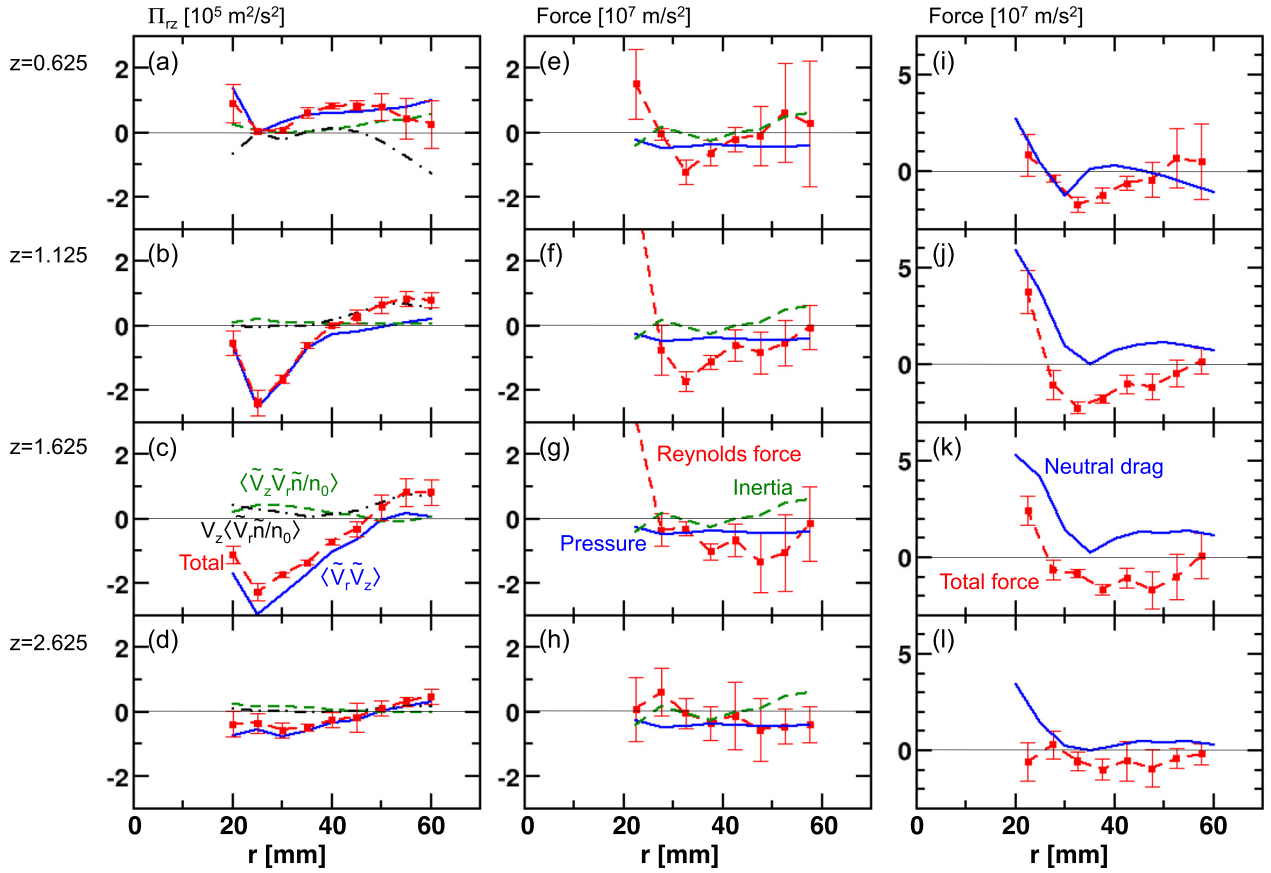

FIG. 5. Radial profiles of (left column) the radial-axial Reynolds stress, (center column) the flow excitation force terms in the force balance equation, and (right column) the total flow excitation force and the neutral drag term for $z = 0.625$ m (top row), 1.125 m (second row), 1.625 m (third row), and 2.625 m (bottom row).

Uncertainty regarding the neutral drag term is somewhat larger, since the data available to evaluate the ion-neutral collision frequency ν_{in} is limited. An order estimation of ν_{in} is given as[32]

$$\nu_{in} = n_e \frac{1-\alpha_i}{\alpha_i} \sigma_{in} v_i \sim 40\,\mathrm{kHz}, \tag{8}$$

where $\alpha_i \sim 0.1$ is the ionization ratio evaluated from the electron density and the neutral density estimated from the neutral pressure, $\sigma_{in} \sim 10^{-18}\,\mathrm{m}^2$ is the ion-neutral collision cross section,[33] and v_i is the ion thermal velocity. The sum of the four flow excitation forces shown in Figs. 5(e)–5(h) and the evaluated neutral drag force are compared in Figs. 5(i)–5(l), respectively. Both the flow excitation force and the drag force take similar shapes in the cases of $z = 0.625$ m, 1.125 m, and 1.625 m, although a constant offset of $\sim 2 \times 10^7\,\mathrm{m/s}^2$ remains in the latter two cases. The sheared parallel flow structure is well explained by the parallel Reynolds stress induced by the drift wave. As shown in Fig. 5(l), the shape of the excitation force and the drag force do not agree, in particular, at $r \sim 20$ mm when the measurement location approaches the end-plate region. In order to discuss the force balance in this region, proper modeling of the end-plate that bounds plasma kinetically and electrically may be necessary. Furthermore, near the end-plate region, the plasma is partially dominated by the recombination process, which can also alter the fluctuation characteristics. These issues are left for future studies.

V. COEXISTENCE OF DENSITY GRADIENT DRIVEN MODE AND PARALLEL FLOW SHEAR DRIVEN MODE

The inward directed particle transport at the inner radii shown in Fig. 4(e) indicates that the drift wave is linearly stable at that region. An alternative candidate of the instability excited there is the D'Angelo mode,[17] whose free energy source is the parallel flow shear. The linear stability analysis including the drift wave coupling with the D'Angelo mode has been undertaken.[22] The key parameter here is $k_\theta k_z \bar{V}'$, where k_z and k_θ are the axial and the azimuthal wavenumbers, respectively, and $\bar{V}'_z$ denotes the parallel flow shear $\partial \bar{V}_z / \partial r$. Depending on the sign of $k_\theta k_z \bar{V}'$, the parallel flow shear either decreases ($k_\theta k_z \bar{V}' > 0$) or increases ($k_\theta k_z \bar{V}' < 0$) the parallel compressibility, which acts to destabilize either the D'Angelo mode or the drift wave. The stability parameter of the D'Angelo mode is given as the marginal stability condition of the linearized fluid equation including the parallel flow shear, as

$$\mathcal{T}_D = \frac{k_z c_s \rho_s k_\theta \bar{V}'_z}{\omega_*^2 / 4\left(1 + k_\theta^2 \rho_s^2\right) + k_z^2 c_s^2}, \tag{9}$$

where ρ_s is the ion sound Larmor radius and ω_* is the drift wave frequency. When $\mathcal{T}_D < 1$, the drift wave dominates the D'Angelo mode, and vice versa. In addition, the inward particle flux is predicted to be possible for the D'Angelo mode, which is brought by the off-diagonal contribution with the parallel flow shear. Figure 6(a) shows the parallel flow shear $\bar{V}'_z$ plotted in the r–z plane. In this discharge,

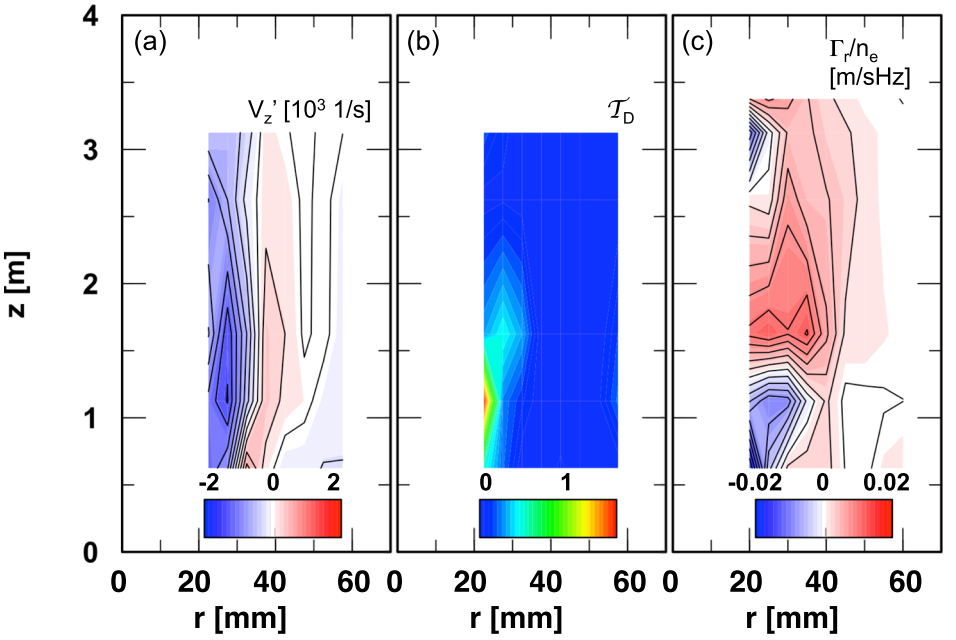

FIG. 6. Spatial distributions of (a) radial derivative of the mean axial velocity, (b) stability parameter of D'Angelo mode, and (c) the mean radial particle flux. Panels (b) and (c) are for the maximum coherent frequency $f \sim 6.4$ kHz.

fluctuations in the drift wave frequency range have $k_z < 0$ and $k_\theta > 0$ in most parts of the plasma column. Thus, $\bar{V}_z' < 0$ is required for the D'Angelo mode to be unstable. This condition is satisfied at $r < 25$ mm. Figure 6(b) is the stability parameter of the D'Angelo mode $\mathcal{T}_D$ at the drift wave frequency region ~6.5 kHz. The stability parameter indicates that the D'Angelo mode is unstable at $r < 25$ mm and $z < 1.6$ m. At these locations, the particle flux is directed inward [shown in Fig. 6(c)], as predicted by the theory. As shown in Sec. IV, the parallel flow shear that drives the D'Angelo mode is originally formed by the momentum transport of the drift wave. Here, the fluctuations and turbulent transport channels are strongly connected, forming a *cross-ferroic turbulence* system.

At the location close to the source region, two different instabilities coexist at different radii. It is worthwhile to analyze the interrelation between the D'Angelo mode at $r < 25$ mm and the drift wave at $r > 25$ mm at $z = 0.625$ m. First, the correlation between them is examined by means of the frequency resolved squared cross coherence analysis. Figure 7 shows the squared cross coherence of the azimuthal electric field fluctuation measured with the Mach probe array against a reference probe at $(r, z) = (40\,\text{mm}, 2.125\,\text{m})$ that measures the density fluctuation. Again, the analysis is performed for the drift wave frequency region ~6.5 kHz. The squared cross coherence profile has at least three distinguishable regions of high coherence: these correspond to the D'Angelo mode at $r \sim 20$ mm, the drift wave at $r \sim 35$ mm, and the higher harmonics of the mediator at $r \sim 60$ mm. Surprisingly, these modes fluctuate maintaining a phase correlation.

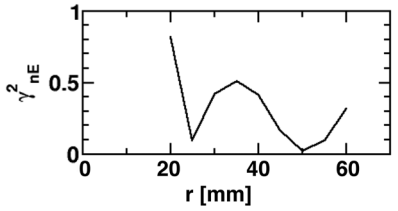

FIG. 7. Radial profile of squared cross coherence between the azimuthal electric field fluctuation at $(z, r) = (0.625\,\text{m}, \text{r})$ and the density fluctuation at $(z, r) = (2.125\,\text{m}, 40\,\text{mm})$.

The causal relation between the D'Angelo mode and the drift wave can be studied by means of the Amplitude Correlation Technique (ATC).[34] Here, the frequency of interest, $5.5\,\text{kHz} \le f \le 7.2\,\text{kHz}$, is extracted by use of a digital filter, and then the time evolution of the envelope signal is obtained by use of the Hilbert transform. Figure 8 shows an example of the filtered signal and its envelope. Two-time and two-point cross correlation function of the envelope signals is defined as

$$C_{1,2}(\tau, r) = \frac{\left[\{e_1(t, r_0) - \bar{e}_1(r_0)\}\{e_2(t+\tau, r) - \bar{e}_2(r)\}\right]_E}{\sqrt{\left[\{e_1(t, r_0) - \bar{e}_1(r_0)\}^2\right]_E}\sqrt{\left[\{e_2(t, r) - \bar{e}_2(r)\}^2\right]_E}}, \tag{10}$$

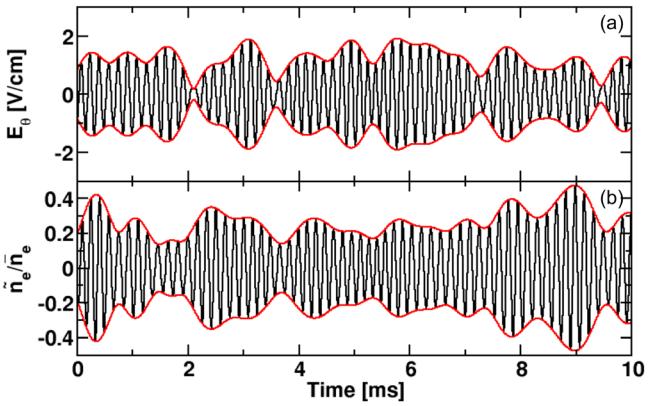

FIG. 8. Time evolution of the filtered signal ($5.5\,\text{kHz} \le f \le 7.2\,\text{kHz}$) and its envelope for (a) the azimuthal electric field fluctuation at $z = 0.625$ m and $r = 20$ mm and (b) the normalized density fluctuation at $z = 1.625$ m and $r = 40$ mm.

where brackets $[*]_E$ denote the ensemble averages, $e_{1,2}$ indicate the envelope of the reference signal and the target signal, and $r_0 = 40$ mm is the radius of the reference probe. Figure 9 shows the cross correlation function $C(\tau, r)$ obtained against the reference probe at $(r, z) = (40\,\text{mm}, 2.125\,\text{m})$, and its time and space slices. Two peaks appear in the cross correlation function at $r = 20$ mm and 35 mm where the D'Angelo mode and the drift wave emerge, respectively. The time difference between two peaks is less than several tens of microseconds, which is much shorter than the fluctuation frequency. It is found that the wave amplitude of these two modes synchronously fluctuate. Note that this result is robust against change of the parameters for the cross correlation function, e.g., the window length.

VI. DISCUSSION

The experimental observations presented so far are summarized in a conceptual diagram shown in Fig. 10. Note that a similar system between the density gradient and the zonal flow shear is found in CSDX.[20] The diagram manifests the experimentally demonstrated relations among the gradients, modes, and fluxes. First, inhomogeneity is provided to the density profile by the plasma source. The density gradient excites the drift wave releasing the free energy. Then, on the one hand, the drift wave forms the outward particle transport as the on-diagonal transport channel, which corresponds to the diffusive damping process. On the other hand, the drift wave induces the parallel momentum transport that enhances the parallel flow shear as an off-diagonal transport channel. The excited parallel flow shear then generates the D'Angelo mode, again releasing its free energy. The D'Angelo mode secondary excited also forms the transport channels in two ways, i.e., the on-diagonal channel and the off-diagonal channel. The former and the latter channels correspond to the viscous damping momentum transport (not discussed here) and the inward particle pinch that steepens the peaked density profile.

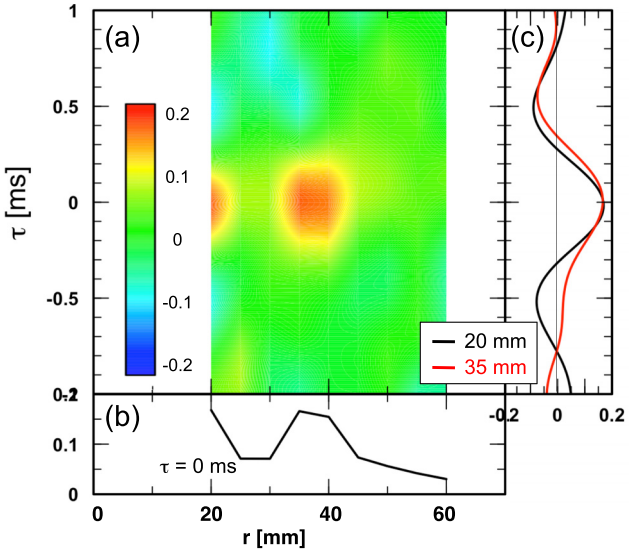

FIG. 9. (a) Two-time and two-point cross correlation function $C(\tau, r)$ between the azimuthal electric field fluctuation at $(z, r) = (0.625\,\text{m}, \text{r})$ and the density fluctuation at $(z, r) = (2.125\,\text{m}, 40\,\text{mm})$, (b) time evolution of the cross correlation function at fixed radii ($r = 20$ mm and 35 mm), and (c) radial profile of the cross correlation function at a fixed time ($\tau = 0$ s).

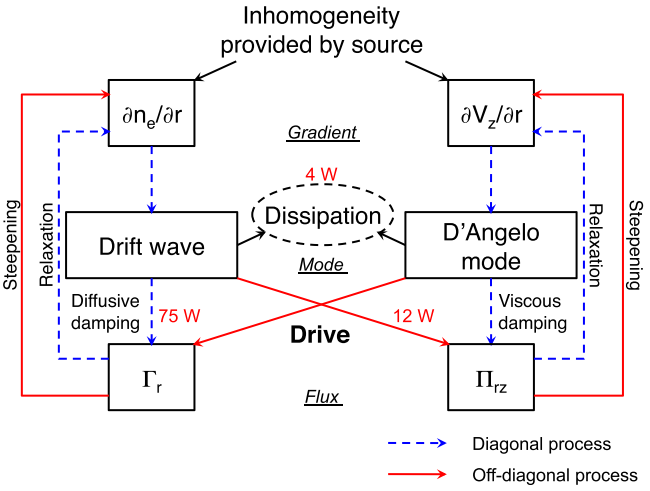

FIG. 10. Conceptual diagram of the cross-ferroic turbulence.

The input energy into the fluctuations is somehow dissipated. Examining the dissipation channels provides quantitative information of the energy partition of the chained structural formation. The energy relaxation densities associated with the particle flux and the parallel momentum flux are defined as

$$w_r = F_r \bar{V}_r = -\frac{\partial p_e}{\partial r}\frac{\Gamma_r}{n_e}, \tag{11}$$

and

$$w_z = F_z \bar{V}_z = -n_i m_i \frac{\partial r \Pi_{rz}}{r \partial r} \bar{V}_z, \tag{12}$$

respectively. In addition, excitation and quenching processes of fluctuations also contribute to the energy dissipation. The order of the energy relaxation density for turbulence dissipation process can be evaluated as

$$w_{\text{turb}} = n_i m_i \langle \tilde{V}_r^2 + \tilde{V}_\theta^2 + \tilde{V}_z^2 \rangle / 2\tau_{\text{corr}}, \tag{13}$$

where $\tau_{\text{corr}} \sim 1$ ms denotes the turbulence correlation time. Figure 11 shows the energy relaxation densities in the r–z plane. The energy relaxation density for the parallel Reynolds stress is localized at the inner radii, where both the parallel flow and the parallel Reynolds stress force are large. The energy relaxation density for the particle flux is distributed throughout the r–z plane. The turbulent energy relaxation density is large at the inner radii and near the source region, but its magnitude is one order smaller than the other two. Volume integrated energy dissipation rate is defined as

$$W_j = \int\int\int w_j r \mathrm{d}r \mathrm{d}\theta \mathrm{d}z, \tag{14}$$

where j indicates r, z, or turb. Note that the integration is performed in $0.625\,\text{m} < z < 3.375\,\text{m}$, $20\,\text{mm} < r < 60\,\text{mm}$, and $0 < \theta < 2\pi$, where the symmetry is assumed in the azimuthal direction. The integrated energy relaxation rates W_r, W_z, and W_{turb} are obtained as 75 W, 12 W, and 4 W, respectively.

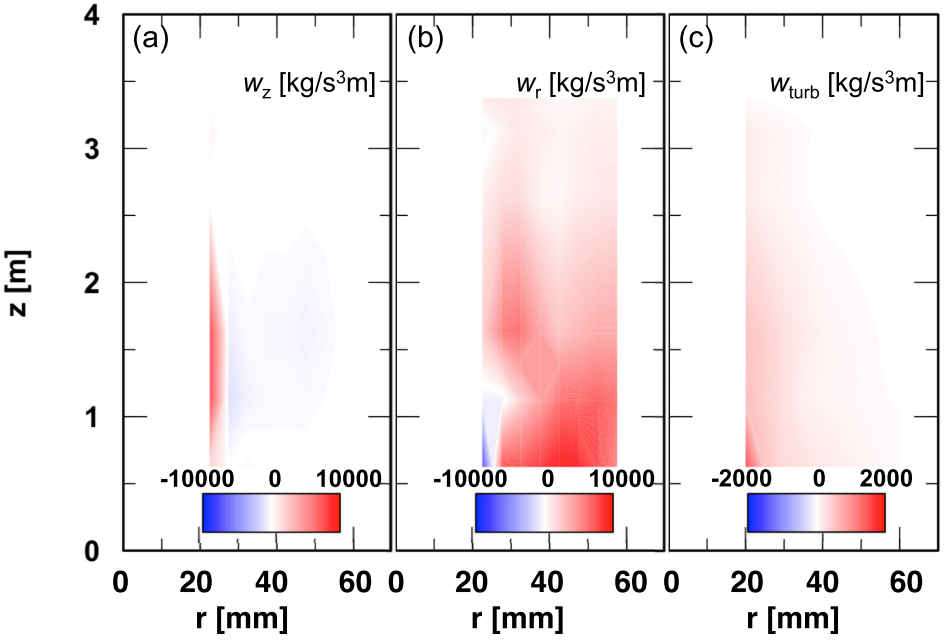

FIG. 11. Energy relaxation densities for (a) the parallel Reynolds stress, (b) the radial particle flux, and (c) turbulence dissipation.

These values are also written in Fig. 10. Therefore, the major energy relaxation channel is the radial particle transport. This result is consistent with our understanding so far, i.e., the original free energy is the density gradient, and the primary instability is the drift wave. Note that for w_z a large contribution of the energy relaxation density may exist at $r < 20$ mm, where the probe cannot access without disturbing the plasma. Assuming that w_z at $r < 20$ mm takes the same value as w_z at $r = 20$ mm, W_z becomes a factor of three larger. This does not alter the conclusion made here.

VII. SUMMARY

In this paper, we have shown the results of the direct measurement of the parallel flow structure and the parallel Reynolds stress in a linear magnetized plasma, in which a complicated parallel flow structures was formed. It was shown that the parallel Reynolds stress induced by the density gradient driven drift wave is the source of the parallel flow structure quantitatively. Moreover, the parallel flow shear generated by the parallel Reynolds stress was found to drive the parallel flow shear driven instability D'Angelo mode, which coexists with the original drift wave. The excited D'Angelo mode induced the inward particle flux, which seems to help in maintaining the peaked density profile. The structure formation in the parallel flow profile and the density profile was discussed in the case where the drift wave and the D'Angelo mode coexists forming the cross-ferroic turbulent state.

ACKNOWLEDGMENTS

We are grateful to Professor P. H. Diamond, Professor A. Fukuyama, and Professor G. R. Tynan for useful discussions. We also thank Professor K. Ida and Professor S. Sakakibara for strong support. This work was partly supported by the Grant-in-Aid for Scientific Research of JSPS (15H02335, 15H02155, 23244113), the collaboration programs of the National Institute for Fusion Science and RIAM Kyushu University (NIFS13KOCT001), and Asada Science Foundation.

[1]K. Itoh, S.-I. Itoh, and A. Fukuyama, *Transport and Structural Formation in Plasmas* (Institute of Physics Publication, 1999).
[2]P. H. Diamond, S.-I. Itoh, and K. Itoh, *Modern Plasma Physics* (Cambridge University Press, 2010), Vol. 1.
[3]J. E. Rice, A. Ince-Cushman, L.-G. Eriksson, Y. Sakamoto, A. Scarabosio, A. Bortolon, K. H. Burrell, B. P. Duval, C. Fenzi-Bonizec, M. J. Greenwald *et al.*, Nucl. Fusion **47**, 1618 (2007).
[4]W. M. Solomon, K. H. Burrell, R. Budny, R. J. Groebner, J. E. Kinsey, G. J. Kramer, T. C. Luce, M. A. Makowski, D. Mikkelsen, R. Nazikian *et al.*, Plasma Phys. Controlled Fusion **49**, B313 (2007).
[5]K. Ida, M. Yoshinuma, K. Nagaoka, M. Osakabe, S. Morita, M. Goto, M. Yokoyama, H. Funaba, S. Murakami, K. Ikeda *et al.*, Nucl. Fusion **50**, 064007 (2010).
[6]E. J. Strait, T. S. Taylor, A. D. Turnbull, J. R. Ferron, L. L. Lao, B. Rice, O. Sauter, S. J. Thompson, and D. Wróblewski, Phys. Rev. Lett. **74**, 2483 (1995).
[7]K. Nagaoka, T. Ishihara, A. Okamoto, S. Yoshimura, and M. Y. Tanaka, J. Plasma Fusion Res. Ser. **4**, 359–362 (2001).
[8]S. Oldenbürger, K. Uriu, T. Kobayashi, S. Inagaki, M. Sasaki, Y. Nagashima, T. Yamada, A. Fujisawa, S.-I. Itoh, and K. Itoh, Plasma Fusion Res. **7**, 2401146 (2012).
[9]Y. Saitou, A. Yonesu, S. Shinohara, M. V. Ignatenko, N. Kasuya, M. Kawaguchi, K. Terasaka, T. Nishijima, Y. Nagashima, Y. Kawai *et al.*, Phys. Plasmas **14**, 072301 (2007).
[10]P. H. Diamond, C. J. McDevitt, Ö. D. Gürcan, T. S. Hahm, W. X. Wang, E. S. Yoon, I. Holod, Z. Lin, V. Naulin, and R. Singh, Nucl. Fusion **49**, 045002 (2009).
[11]P. H. Diamond, Y. Kosuga, Ö. D. Gürcan, C. J. McDevitt, T. S. Hahm, N. Fedorczak, J. E. Rice, W. X. Wang, S. Ku, J. M. Kwon *et al.*, Nucl. Fusion **53**, 104019 (2013).
[12]C. Hidalgo, B. Gonçalves, C. Silva, M. A. Pedrosa, K. Erents, M. Hron, and G. F. Matthews, Phys. Rev. Lett. **91**, 065001 (2003).
[13]B. Gonçalves, C. Hidalgo, M. A. Pedrosa, R. O. Orozco, E. Sánchez, and C. Silva, Phys. Rev. Lett. **96**, 145001 (2006).
[14]B. Labit, C. Theiler, A. Fasoli, I. Furno, and P. Ricci, Phys. Plasmas **18**, 032308 (2011).
[15]S. H. Müller, J. A. Boedo, K. H. Burrell, J. S. deGrassie, R. A. Moyer, D. L. Rudakov, and W. M. Solomon, Phys. Rev. Lett. **106**, 115001 (2011).
[16]Y. Xu, C. Hidalgo, I. Shesterikov, M. Berte, P. Dumortier, M. Van Schoor, M. Vergote, A. Krämer-Flecken, R. Koslowski, and TEXTOR Team, Nucl. Fusion **53**, 072001 (2013).
[17]N. D'Angelo, Phys. Fluids **8**, 1748–1750 (1965).

[18]T. Kaneko, H. Tsunoyama, and R. Hatakeyama, Phys. Rev. Lett. **90**, 125001 (2003).
[19]G. Wang, L. Wang, X. Yang, C. Feng, D. Jiang, and X. Qi, Plasma Phys. Controlled Fusion **40**, 429 (1998).
[20]L. Cui, G. R. Tynan, P. H. Diamond, S. C. Thakur, and C. Brandt, Phys. Plasmas **22**, 050704 (2015).
[21]S. Inagaki, T. Kobayashi, Y. Kosuga, S.-I. Itoh, T. Mitsuzono, Y. Nagashima, H. Arakawa, T. Yamada, Y. Miwa, N. Kasuya *et al.*, Sci. Rep. **6**, 22189 (2016).
[22]Y. Kosuga, S.-I. Itoh, and K. Itoh, Plasma Fusion Res. **10**, 3401024 (2015).
[23]S. Shinohara, T. Hada, T. Motomura, K. Tanaka, T. Tanikawa, K. Toki, Y. Tanaka, and K. P. Shamrai, Phys. Plasmas **16**, 057104 (2009).
[24]M. Hudis and L. M. Lidsky, J. Appl. Phys. **41**, 5011 (1970).
[25]B. J. Peterson, J. N. Talmadge, D. T. Anderson, F. S. B. Anderson, and J. L. Shohet, Rev. Sci. Instrum. **65**, 2599–2606 (1994).
[26]S. Kado, T. Shikama, S. Kajita, T. Oishi, and S. Tanaka, Contrib. Plasma Phys. **44**, 656–661 (2004).
[27]I. H. Hutchinson, Phys. Rev. A **37**, 4358 (1988).
[28]T. Yamada, S.-I. Itoh, K. Terasaka, N. Kasuya, Y. Nagashima, S. Shinohara, T. Maruta, M. Yagi, S. Inagaki, Y. Kawai, A. Fujisawa, and K. Itoh, Plasma Fusion Res. **3**, S1021–S1021 (2008).
[29]T. Yamada, S-I. Itoh, T. Maruta, N. Kasuya, Y. Nagashima, S. Shinohara, K. Terasaka, M. Yagi, S. Inagaki, Y. Kawai *et al.*, Nat. Phys. **4**, 721–725 (2008).
[30]T. Yamada, S.-I. Itoh, S. Inagaki, Y. Nagashima, S. Shinohara, N. Kasuya, K. Terasaka, K. Kamataki, H. Arakawa, M. Yagi *et al.*, Phys. Plasmas **17**, 052313 (2010).
[31]T. Yamada, S.-I. Itoh, S. Inagaki, Y. Nagashima, N. Kasuya, K. Kamataki, H. Arakawa, T. Kobayashi, M. Yagi, A. Fujisawa, and K. Itoh, Phys. Rev. Lett. **105**, 225002 (2010).
[32]N. Kasuya, M. Yagi, M. Azumi, K. Itoh, and S.-I. Itoh, J. Phys. Soc. Jpn. **76**, 044501 (2007).
[33]A. V. Phelps, J. Phys. Chem. Ref. Data **20**, 557 (1991).
[34]T. Yamada, S.-I. Itoh, S. Inagaki, Y. Nagashima, K. Kamataki, H. Arakawa, M. Yagi, A. Fujisawa, and K. Itoh, J. Phys. Soc. Jpn. **79**, 085001 (2010).